Desalination and Water Treatment
www.deswater.com

doi: 10.5004/dwt.2019.23784

148 (2019) 285–295
April

Preparation of $C/CoFe_2O_4$ nanocomposites based on membrane dispersion-hydrothermal carbonization and their application for dyeing removal

Min Lu[a], Qian Wu[a], Xiao-Hui Guan[a], Qi-Yuan Zheng[a], Guang-Sheng Wang[b,*]

[a]*School of Chemical Engineering, Northeast Electric Power University, Jilin 132000, P. R. China, email: lumin19770919@163.com (M. Lu), 1060200601@qq.com(Q. Wu), guanxh@neepu.edu.cn (X.-H. Guan), 11720065351@qq.com(Q.-Y. Zheng)*
[b]*School of Chemistry, Beihang University, Beijing 100191, PR China, email: wanggsh@buaa.edu.cn (G.-S. Wang)*

Received 24 April 2018; Accepted 12 January 2019

ABSTRACT

The novel carbon-encapsulated magnetic nanoparticles (CEMNPS)-$C/CoFe_2O_4$ have been synthesized by the double-membrane dispersion technology and the hydrothermal carbonization method in mild condition with absolutely green process. The magnetic property of composites reveals its excellent magnetic performance in the dye removal. As the absorbents, they are employed for anionic dyes removal Congo red from aqueous solutions. The results indicate that the composites show excellent adsorption efficiency performance and the adsorption quantity of Congo red is 43.07 mg/g. The enhanced adsorption mechanism was explained by the isothermal, thermodynamic and kinetic studies, the results confirm that the adsorption process is favourable, exothermic and spontaneous. Our result implies that the $C/CoFe_2O_4$ composites can be effectively applied for the removal of pollutant as potential adsorbents.

Keywords: Nanomaterial; Dye removal

1. Introduction

During the manufacture process of dyeing and printing process, it is estimated that 10–30% of organic raw materials would be transferred to wastewater. Because of hazard and toxicity to human and otherworldly livings, water contamination resulted from dyeing and finishing in textile industry has been of primary environmental concern [1–5]. Several conventional techniques such as a bio-degradation process [6], a electrochemcial technique [7,8], homogeneous and heterogeneous photocatalytic oxidation [9,10] have been widely applied for the treatment of dyes from wastewater. Among the techniques, adsorption method appears to be the most effective, especially for effluents with moderate and low concentration [11–14]. Different adsorbents are eligible for this purpose. Activated carbon is the most popular adsorbent and has been used with great success in the wastewater treatment [15–17]. However, the activated carbon is considered one of the expensive adsorbents, which limits further application especially in the developing countries. Therefore, based on the properties of carbonaceous materials, the hot topic of present study is to explore preparation method with high carbon yield and low cost.

On the other hand, magnetic nanoparticles can be conveniently separated from wastewater with the help of an external magnet because of excellent magnetic properties [18–21]. Therefore, it has been suggested that carbon-encapsulated magnetic nanoparticles (CEMNPS) have potentials as a novel magnetic nano-adsorbent for the efficient removal of dyes due to their unique physicochemical properties [22–26]. Different derived metal oxide doped nano-sized activated carbons are considered as prospective adsorbents for aqueous pollutants. Lunhong Ai et al. have synthesized carbon/$CoFe_2O_4$ magnetic composite for the removal of malachite green dye [27]. And Thangamani K.S. et al. brought to coat dung activated carbon/$CoFe_2O_4$ for the adsorption of anionic dyes Direct Brown 2 and Reactive Red 152 [28]. $CoFe_2O_4$ applied in numerical examples is proved to be remarkable because of saturation magnetization, excellent chemical stability and mechanical hardness

*Corresponding author.

[29–33]. However, there are also insufficient in conventional methods of $CoFe_2O_4$ such as nonuniform in size and distribution, high cost and discontinuous preparation.

In this work, we firstly reported an efficient, low cost method to synthesize $C/CoFe_2O_4$ nanocomposites by double-membrane dispersion technology and hydrothermal carbonization method in relatively mild conditions, absolutely green process [34,35]. Subsequently, they were employed to adsorb Congo red in wastewater. The adsorption efficiency and mechanism were investigated in details. We attempted to provide economically feasible and easy industrial-production method to synthesize $C/CoFe_2O_4$ for developing their applications in magnetically separable adsorbents.

2. Experiment

2.1. The preparation of $CoFe_2O_4$ and $C/CoFe_2O_4$ nanocomposites

All chemicals were of analytical grade and used as received without further purification. The preparation of nanometer $CoFe_2O_4$ precursors was based on membrane dispersion technology (Fig. S1). In a typical synthesis, the concentration of Fe^{3+} and Co^{2+} mixture was 0.4 mol/L, and the ratio of Fe^{3+} and Co^{2+} was 2:1. 0.5 mol/L of $H_2C_2O_4$ solution and the mixed solution of Fe^{3+} and Co^{2+} were simultaneously sent into the membrane module by peristaltic pump. Then, the mixture was transferred into an autoclave, which was tightly sealed and hydrothermally treated at 120 °C for 24 h in an oven. The product was washed with deionized water and absolute ethanol several times, and dried in air at 80°C for 10 h. Next, the $CoFe_2O_4$ precursor was transferred into the porcelain boat, heated in a muffle furnace at the rate of 5°C/min and calcined at 550°C for 2 h. Finally, the product, $CoFe_2O_4$, was obtained after cooling.

Under magnetic stirring, the above prepared $CoFe_2O_4$, a certain proportion of caboxymethyl cellulose (CMC) and 0.03 g of CTAB were added to this system in the following step to form a stable solution, and then transferred into a 100 mL Teflon-lined stainless steel autoclave and subsequently sealed and heated for several hours in an oven. After reaction, the autoclave was cooled to room temperature. Afterward, the black precipitate was centrifuged at 3000 rpm and washed 6 times using deionized water, ethanol. Finally, the product was dried in vacuum oven at 60°C for 10 h, and after that, the product, $C/CoFe_2O_4$, was obtained.

2.2. Characterization

The morphology and size of the samples were obtained by scanning electron microscopy (SEM, Quanta200, Holland). The crystallization of the products was examined by X-ray diffraction (XRD, XRD-7000, Japan) with Cu-KR radiation. The changes of functional groups before and after hydrothermal carbonization were measured using Fourier transform infrared spectroscopy (FT-IR, IRPrestige-21, Japan). The elemental composition of the products was determined using energy dispersive X-ray spectroscopy (EDS, INCA-250, Japan). The specific surface area of samples was tested on volumetric gas sorption instrument (BET, ASAP2020, America).

2.3. Measurement of adsorption properties

To measure the adsorption properties of different materials with the following procedure, the adsorption experiments were carried out in the thermostatic oscillator. 0.02 g of adsorbent material (C, $CoFe_2O_4$, $C/CoFe_2O_4$) was added into 20 mL of different initial concentrations of Congo red dye. After vibration at a fixed temperature for certain reaction time, the mixtures were centrifuged prior to measure the concentration of the final solutions by UV-visible spectrophotometer (UV-2550, Japan) at 500 nm.

3. Results and discussion

3.1. Morphology and structure analysis of samples

The XRD pattern of $CoFe_2(C_2O_4)_3{\cdot}6H_2O$ as the precursor of $CoFe_2O_4$ shows that all diffraction peaks are in good agreement with the 9 crystal planes of $CoFe_2(C_2O_4)_3$ (Fig. S2) , which is consistent with the result of the other literature [36]. After calcination at high temperature, $CoFe_2O_4$ was formed by lost crystal water of $CoFe_2(C_2O_4)_3$. The synthesis of Co-Fe oxalate precursor could be formulated as Eqns. (1) and (2).

$$Co^{2+} + 2Fe^{2+} + 3C_2O_4^{2-} + 6H_2O \rightarrow CoFe_2(C_2O_4)_3 \cdot 6H_2O \quad (1)$$

$$CoFe_2(C_2O_4)_3 \cdot 6H_2O \rightarrow CoFe_2O_4 + 2CO_2 + 4CO + 6H_2O \quad (2)$$

Fig. 1a shows that the characteristic peak of carbon appeared at 2θ = 44°, as indicates that hydrothermal carbonization microspheres is synthesized. Fig. 1b shows that the diffraction peaks can be indexed to the reflection of (104), (113), (024), (214), (125), and (208) planes, respectively, which is a pure cubic spinel phase $CoFe_2O_4$ (JCPDS No. 79-1744) [37]. $C/CoFe_2O_4$ nanocomposites were obtained through hydrothermal carbonization of the as-prepared $CoFe_2O_4$ in an oven at 180°C for 12 h, and the XRD patterns of nanocomposites with different ratio of reactants are shown in Figs. 1c, d and e, respectively.

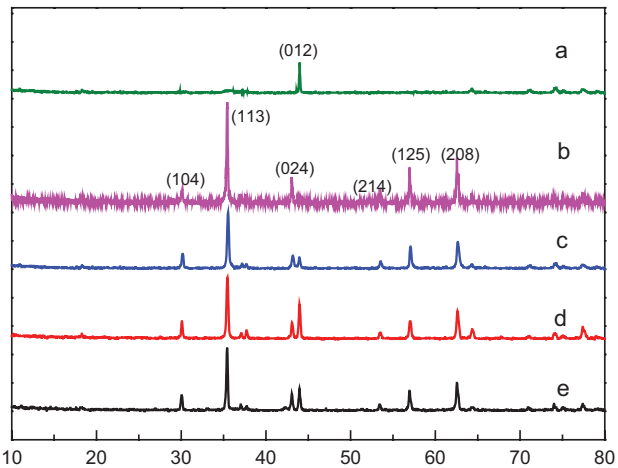

Fig. 1. XRD pattern of C, $CoFe_2O_4$ and $C/CoFe_2O_4$ nanocomposites. C; (b) $CoFe_2O_4$; (c) $C/CoFe_2O_4$, 180°C, $mCoFe_2O_4$:mC = 1:1; (d) $C/CoFe_2O_4$, 180°C, $mCoFe_2O_4$:mC = 1:2; (e) $C/CoFe_2O_4$, 180°C, $mCoFe_2O_4$:mC = 1:3.

The SEM image (Fig. 2a) indicates that the as-prepared $CoFe_2O_4$ product with rod-like nanostructure consists of uniform and disperse materials. Large quantities of uniform nanorods are approximately 800 nm. The reaction temperature is one of the key factors involved in this reaction. The SEM images of $C/CoFe_2O_4$ nanocomposites are shown in Figs. 2b–d. The diameter of the nanorods was significantly increased to about 2.5 μm. Hydrothermal carbonization microspheres of CMC had been successfully loaded on the surface of $CoFe_2O_4$ nanorods at different temperature. When the reaction temperature was 180°C, the distribution of nanocomposites was uniform and no obvious agglomeration phenomenon was observed (Fig. 2b). By contrast, $CoFe_2O_4$ nanorods were more finely dispersed and uneven particles with the increase of the hydrothermal temperature (Figs. 2c and 2d). While CMC would be not hydrothermal carbonized into spherical shapes below 180°C. Therefore, the optimized reaction temperature is 180°C. To learn more about the impact of ratio of reactants, we also investigated the research of mass ratio of $CoFe_2O_4$ and CMC (Figs. 2e and 2f) at 180°C for 6 h. It was interesting that the effect of the ratio of reactant was not distinct. The composition of the as-prepared sample was verified by EDS spectroscopy (shown in inset of Fig. 2f), which shows the nanocomposites contain only Co, Fe, C and O, and the whole nanostructures are uniform.

TEM images are shown in Fig. 3. It is observed that the microspheres have been shaped on the $CoFe_2O_4$. After hydrothermal carbonization, the diameter of nanocomposites increased to 1 μm, which was bigger than that of $CoFe_2O_4$. The size differences of nanocomposites in TEM and SEM may be due to the superposition of several single $C/CoFe_2O_4$ nanorods. Additional, SAED pattern of the nanocomposites is shown in Fig. 3 (inset diagram). Appearance of the diffraction rings and spots confirms a high crystalline nature and a polycrystalline nature.

FT-IR spectrums of CMC and $CoFe_2O_4$ before and after hydrothermal carbonization are shown in Fig. S3. The bands of CMC before and after carbonization were almost same in FT-IR spectra. After carbonization, there were also the existence of the adsorption bands in the range of 3000–3700 cm^{-1} attributed by –OH stretching vibration of water molecules and 3000–2800 cm^{-1} attributed by C-H stretching vibrations of aliphatic. However, the adsorption peaks in the range of 1000–1440 cm^{-1} assigned to C-OH stretching vibration and –OH bending vibration were weak or disappear and the peak at 1690 cm^{-1} assigned to C=O stretching of –COOH group increased, indicating the existence of dehydra-

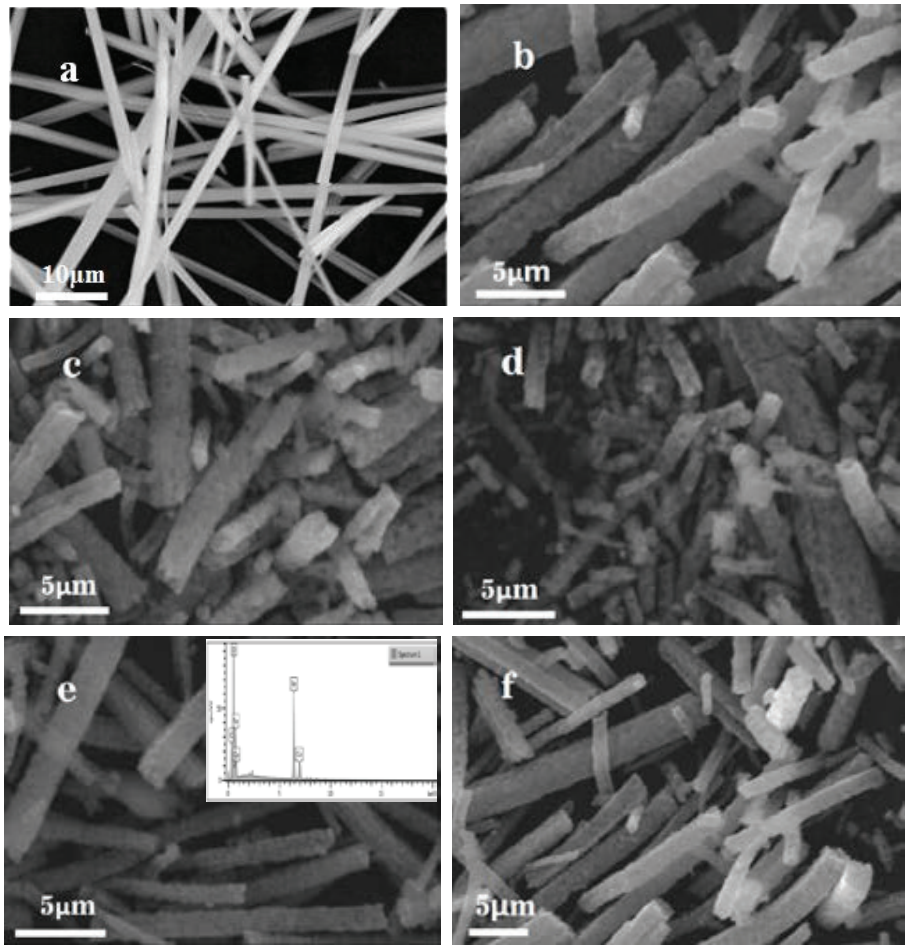

Fig. 2. SEM images of $CoFe_2O_4$ and nanocomposites(a) $CoFe_2O_4$; (b) $C/CoFe_2O_4$, 180°C, $mCoFe_2O_4$:mC = 1:1; (c) $C/CoFe_2O_4$, 200°C, $mCoFe_2O_4$:mC = 1:1; (d) $C/CoFe_2O_4$, 220°C, $mCoFe_2O_4$:mC = 1:1; (e) $C/CoFe_2O_4$, 180°C, $mCoFe_2O_4$:mC = 1:2; (f) $C/CoFe_2O_4$, 180°C, $mCoFe_2O_4$:mC = 1:3; the inset is the EDS of nanocomposites.

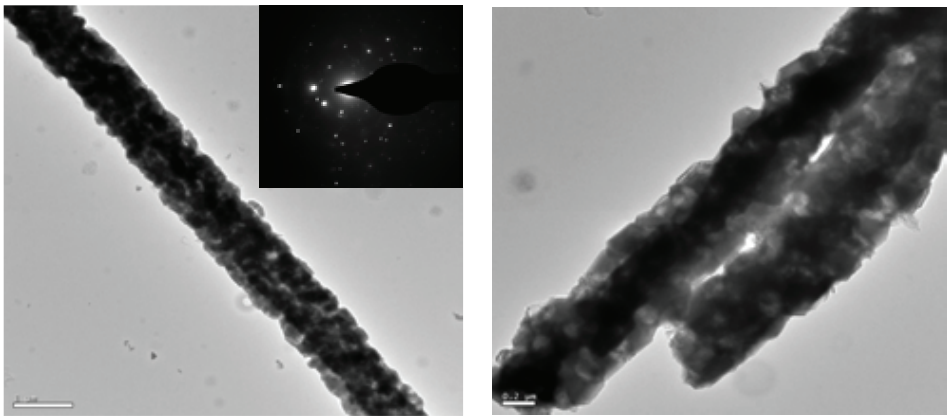

Fig. 3. TEM images of nanocomposites (180°C, m$CoFe_2O_4$:mC = 1:2; the inset is the SAED pattern of nanocomposites.

tion during the hydrothermal carbonization. Meanwhile, adsorption peak at 1620 cm^{-1} attributed by C=C stretching vibration indicates that the existence of aromatization reaction. There were he peaks at 565 cm^{-1} attributed to the stretching vibration of $CoFe_2O_4$ Lattice octahedron. It was suggested that crystal structure of $CoFe_2O_4$ was not destroyed at the process of hydrothermal carbonization [38]. The peaks at 3450 cm^{-1} and 1635 cm^{-1} were the stretching and bending vibration of –OH in the water, respectively [39,40]. After hydrothermal carbonization, the stretching vibration of nanocomposites was red shifted, and the adsorption peak of –OH was increased, indicating that a large amount of –OH had been formed at the surface of nanocomposites [41]. The adsorption peaks located at 2972 cm^{-1} and 1087 cm^{-1} were ascribed to C-H and –COOH formed, respectively. It showed that the spherical activated carbon prepared via hydrothermal carbonization using CMC as starting materials was successfully coated on the surface of $CoFe_2O_4$ [42,43].

N_2 adsorption-desorption isotherms of $CoFe_2O_4$ and C/$CoFe_2O_4$ are presented in Fig. 4. The composite displays the typical type-4 isotherm with the hysteresis loop at a relative pressure range of 0.8–1.0, which demonstrates the mesoporous structure. The BET surface area of the $CoFe_2O_4$ nanorods was 18.57 m^2/g. The BET surface area of C/$CoFe_2O_4$ nanocomposites at 180°C and C/$CoFe_2O_4$ nanocomposites at 200°C were 29.85 m^2/g and 26.12 m^2/g, respectively.

The hysteresis loops of the as-synthesized samples were also measured at 300 K (Fig. 5). At 300 K, the saturation magnetization of $CoFe_2O_4$ nanorods and C/$CoFe_2O_4$ nanocomposites were 96.64 emu/g and 66.10 emu/g, respectively. It indicates that the nanocomposites as absorbent can be easily separated from dye wastewater by magnetic separation techniques [44]. The decrease in saturation magnetization after hydrothermal carbonization was most likely attributed to the decrease in $CoFe_2O_4$ quantity [45].

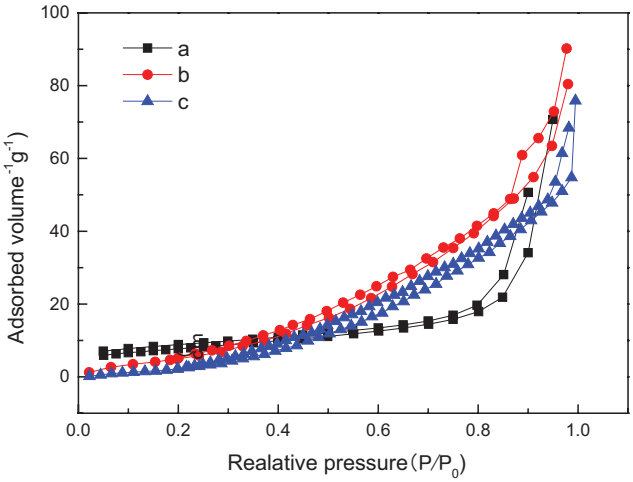

Fig. 4. N_2 adsorption-desorption isotherms for $CoFe_2O_4$ and C/$CoFe_2O_4$ (a) $CoFe_2O_4$; (b) C/$CoFe_2O_4$ 180°C m$CoFe_2O_4$:mC = 1:2; (c) C/$CoFe_2O_4$ 200°C m$CoFe_2O_4$:mC = 1:2.

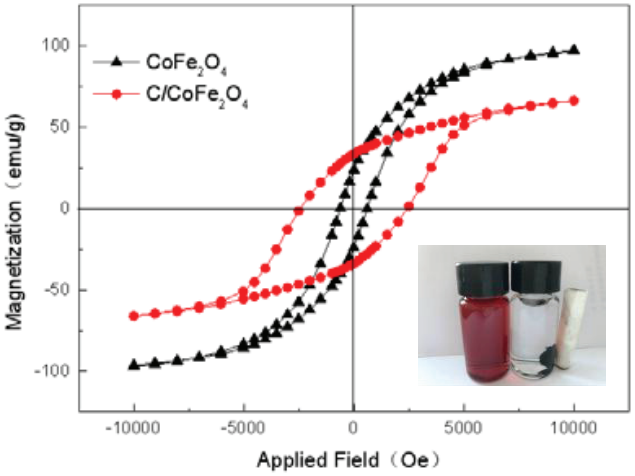

Fig. 5. Magnetic hysteresis loops for $CoFe_2O_4$ and C/$CoFe_2O_4$ (reaction temperature: 180°C, m$CoFe_2O_4$:mC = 1:2).

3.2. The adsorption properties

3.2.1. Effect of the ratio of $CoFe_2O_4$ and CMC

Next, we investigated how the C/$CoFe_2O_4$ nanocomposites behave as absorbents for dye. Fig. 6 shows the effect of

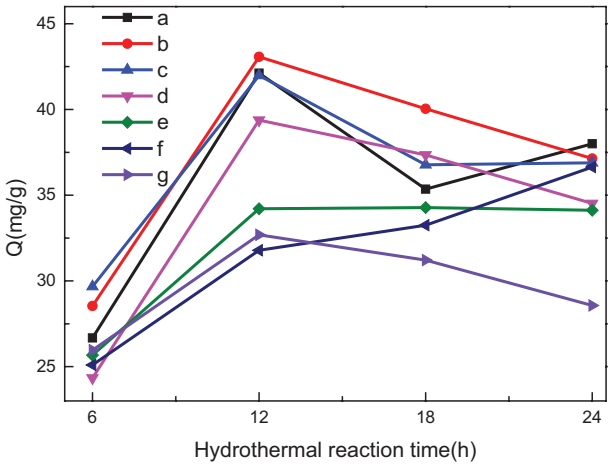

Fig. 6. Adsorption of Congo red dye by nanocomposites. (a) 180°C, mCoFe$_2$O$_4$:mC = 1:1; (b) 180°C, mCoFe$_2$O$_4$:mC = 1:2; (c) 180°C, mCoFe$_2$O$_4$:mC = 1:3; (d) 200°C, mCoFe$_2$O$_4$:mC = 1:1; (e) 200°C, mCoFe$_2$O$_4$:mC = 1:2; (f) 200°C, mCoFe$_2$O$_4$:mC = 1:3; (g) microspheres of CMC after hydrothermal carbonization, 180°C.

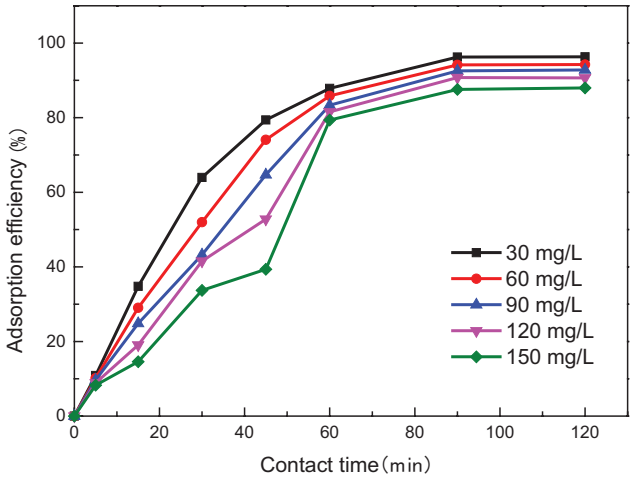

Fig. 7. Effect of initial concentration on adsorption.

the ratio of CoFe$_2$O$_4$ and CMC on the adsorption efficiency. It can be seen that the adsorption capacity of C/CoFe$_2$O$_4$ nanocomposites for Congo red were normally higher than that of CMC after hydrothermal carbonization. It is known that reaction temperature and time are important factors to affect the carbonized porosity. Carbonized porosity of nanocomposites raised with the increasing of temperature and time, which would lead to the increasing of adsorption capacity. When the temperature and time were too high, the adsorption capacity decreased. The reason might be more oxygen groups (OH) of carbohydrates fall off in the form of water in the process of hydrothermal carbonization to decrease the rate of hydrothermal carbon. Therefore, the experimental conditions determined in the subsequent experiments are 180°C and the ratio of 1:2 for 12 h.

3.2.2. *Effect of initial dye concentration*

As the initial concentration (30–150 mg/g) increased, the adsorption efficiency decreased as shown in Fig. 7. It indicated that the dye molecules were heavily dependent on the adsorption sites on the adsorbent during the adsorption process. As the dye concentration increased, the adsorption process would slowly stabilize, which could be attributed to the competition of the dye molecules in the null reaction position. The lower concentration of the dye, the higher the vacancy rate of the adsorbent to the dye, resulting in the increasing for color removal. Similar reports have been made by fly ash and sawdust [46,47]. And the contact time was an importance factor for the adsorbent-adsorption system to reach equilibrium. It can be seen that the adsorption capacity of C/CoFe$_2$O$_4$ materials for Congo red dye reached the maximum adsorption amount at 90 min; and the adsorption rate did not obviously reach with the increasing of time, as indicated that the adsorption reaction reached equilibrium.

In order to describe the adsorption mechanism, the Langmuir, Freundlich and Langmuir-Freundlich and Dubinin-Raduskevich equations were used to analyze the experimental data, which are given in Eqs. (3)–(7) [24,48–50].

$$\frac{C_e}{Q_e} = \frac{C_e}{Q_0} + \frac{1}{K_a Q_0} \tag{3}$$

$$\ln Q_e = \ln K_f + n \ln C_e \tag{4}$$

$$\frac{Q_e}{Q_0} = \frac{K_b C_e^n}{1 + K_b C_e^n} \tag{5}$$

$$\ln Q_e = \ln Q_0 - BA^2 \tag{6}$$

$$A = RT \ln(1 + 1/C_e) \tag{7}$$

where Q_e (mg/g) is the equilibrium adsorption amount; Q_0 (mg/g) is the maximum adsorption capacity; C_e (mg/L) is the equilibrium concentration of Congo red in solution, and K_a, K_f and K_b (L/mg) are the adsorption equilibrium constants of Langmuir, Freundlich and Langmuir-Freundlich equations, respectively; n is a constant depicting the adsorption intensity. k_{DR} is the maximum adsorption capacity in mol/g, B is a constant related to the adsorption related to the adsorption energy in mol^2/J^2 and is calculated from plotting lnQ_e against A^2; A (J/mol) is Polanyi adsorption potential energy, defined as the work done by 1 mol molecular adsorbed from infinity to the distance x between adsorbate and adsorbent surface.

The fitting results are shown in Fig. S4 and Table 1. As shown in Table 1, the Langmuir-Freundlich model could provide best representation of the adsorption isotherms of Congo red than the Langmuir model and Freundlich model. It also confirms the adsorbents have the characteristics of multiphase and asymmetry after hydrothermal carbonization due to the decrease of crystallinity.[24] Although the fitting results of Langmuir model were not as good as that of Langmuir-Freundlich model, the dimensionless constant separation factor or equilibrium parameter RL can be calculated by K_L from Eq. (8) in order to further quantify the adsorption properties [51].

Table 1
Fitting parameters of adsorption isotherms models

Adsorption isotherm models	Constants	Values
Langmuir model	K_L(L/mg)	0.018
	Q_0 (mg/g)	71.83
	R^2	0.9777
Freundlich model	K_F (L/mg)	4.44
	n	0.51
	R^2	0.8828
Langmuir-Freundlich model	K_b (L/mg)	0.011
	Q_0 (mg/g)	53.48
	n	–1.00
	R^2	0.9941
D-R model	K_{DR} (mg/g)	70.81
	B (KJ^2/mol^2)	0.0058
	R	0.9814

$$R_L = 1/(1+K_L C_0) \tag{8}$$

where R_L is the dimensionless constant separation factor; K_L (L/mg) is the Langmuir constant; C_0 (mg/L) is the initial concentration of Congo red in the solution. Because of positive values of K_L, the values of R_L are in the range of 0 to 1, indicating the suitability of the process. *D-R* isotherm is insufficient to explain the chemical and physical properties of the adsorption process. However, the mean adsorption energy (E, kJ/mol) can be calculated from the *B* value of the *D-R* isotherms using the following equation [52].

$$E = 1/(2B)^{1/2} \tag{9}$$

For $E \leq 8$ kJ/mol, physisorption being dominated the adsorption mechanism. If E is in the range 8–16 kJ/mol, the adsorption process follows chemisorption mechanism. The value of E was 9.26 kJ/mol, which indicated that adsorption of Congo red on nanocomposites probably proceed via chemisorption mechanism. The strength of bonding between the dye and nanocomposites clearly decreases as the temperature increases.

3.2.3. Effect of contact time

The absorbance of Congo red dye was measured by UV-Vis spectrophotometer as shown in Fig. 8 The results showed that the absorbance of Congo red dye decreased with the time, indicating that the color group in the dye reacts with the C/$CoFe_2O_4$ material [28]. When the reaction was carried out for 90 min, the absorbance of the dye changed to zero gradually, indicating that the adsorption reaction was balanced, which is consistent with the above discussion.

The adsorption kinetics could describe the rate of adsorbate on adsorbent, which controls the residence time of adsorbate at the solid-solution interface. In order to examine the adsorption mechanisms, *pseudo-first-order*, *pseudo-second-order*, Elovich and intraparticle diffusion kinetic

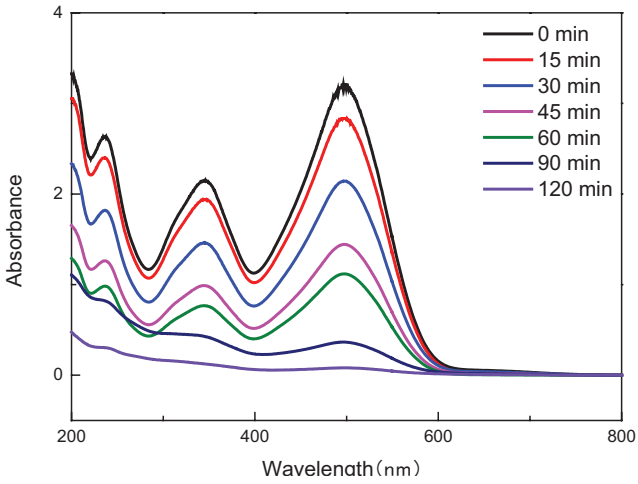

Fig. 8. The absorbance of Congo red dye at different times.

models were used to analysis the experimental data in the study [41,53], which are given as Eqs.(10)–(13). The best-fit model was selected based on the linear regression correlation coefficient (R^2).

$$\ln(Q_e - Q_t) = \ln Q_e - k_1 t \tag{10}$$

$$\frac{t}{Q_t} = \frac{1}{k_2 Q_e^2} + \frac{t}{Q_e} \tag{11}$$

$$Q_t = A + k_e \ln t \tag{12}$$

$$Q_t = k_d t^{1/2} + C \tag{13}$$

where Q_t (mg/g) is adsorption capacity at a time t (min); k_1 (min^{-1}) and k_2 (g/mg·min) are the constants of pseudo-first-order and pseudo-second-order kinetics, respectively; k_e and A are the constants of Elovich equation; k_d is the constant of intra-particle diffusion equation; C is the constant of intraparticle diffusion equation.

Fig. 9 and Table 2 show adsorption kinetics fitting results of Congo red on C/$CoFe_2O_4$ adsorbent. *Pseudo-second-order* model was fittest to the experimental data than other models. These all implied that chemical interactions were involved in the adsorption process, and that there were strong interactions between Congo red and carbonaceous adsorbent. Generally, any adsorption process involves three main successive transport steps, i.e. film diffusion, intraparticle or pore diffusion and adsorption onto interior sites. The value of C was not zero in intraparticle diffusion model, which indicates that intraparticle or pore diffusion is not the only rate-controlling step during the adsorption process.

3.2.3. Effect of temperature

Effect of temperature is a significant physico-chemical process parameter, since temperature influences adsorption capacity. The changes of the adsorption capacity of Congo red dye with the initial concentration of dye were measured

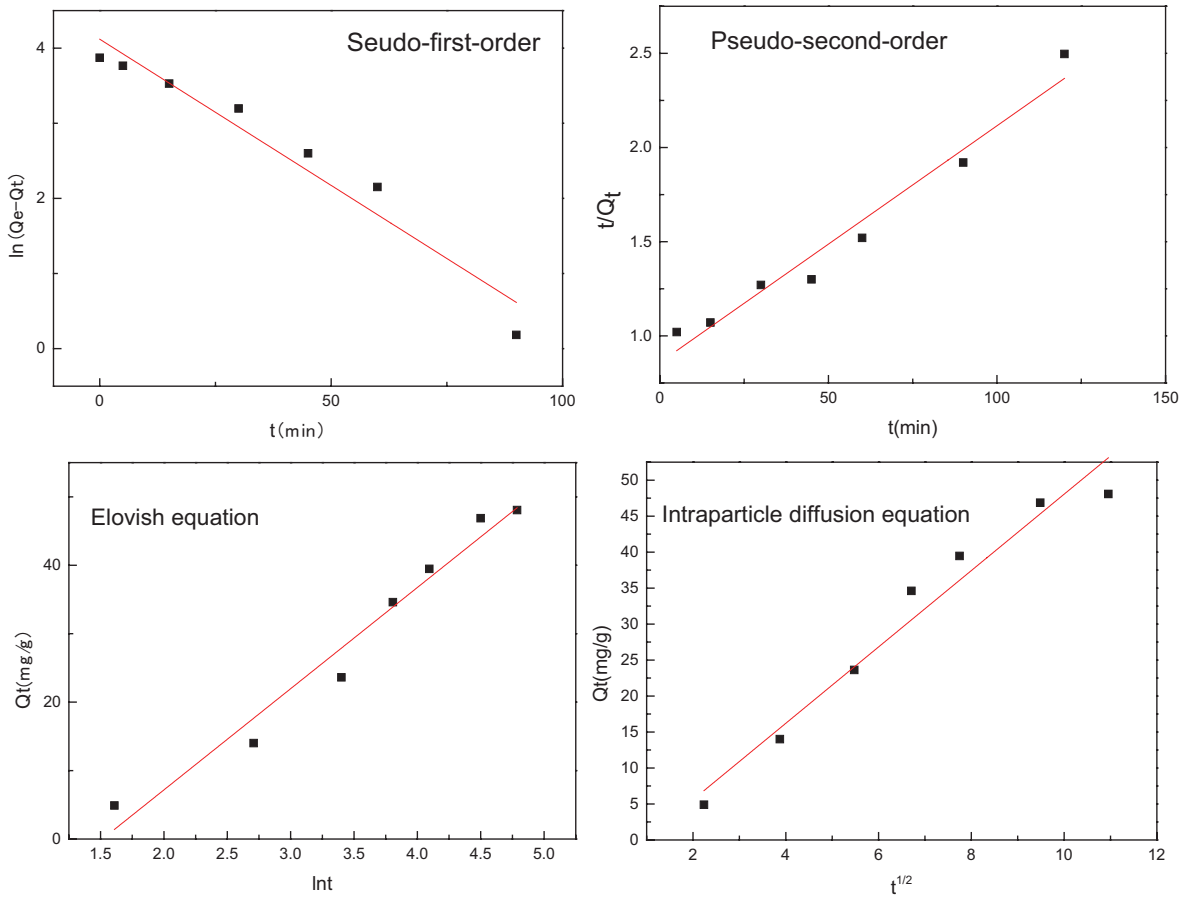

Fig. 9. Kinetic model of congo red adsorbed on nanocomposites.

Table 2
Adsorption kinetic constants and values

Adsorption kinetics models	Constants	Values
Pseudo-first-order	Q_e (mg/g)	46.81
	k_1 (min^{-1})	0.0557
	R^2	0.9640
Pseudo-second-order	Q_e (mg/g)	48.95
	k_2 (g·mg^{-1}·min^{-1})	0.0002
	R^2	0.9932
Elovich equation	A	–22.39
	k_e (min^{-1})	14.79
	R^2	0.9611
Intraparticle diffusion equation	C	–5.01
	k_d (min^{-1})	5.31
	R^2	0.955

at three different temperatures. It can be seen from Fig. 10 that the adsorption capacity increased first, then increased with the increase of the initial concentration of the dye. The temperature increased and the adsorption capacity increased, indicating that high temperature contributes to the occurrence of adsorption.

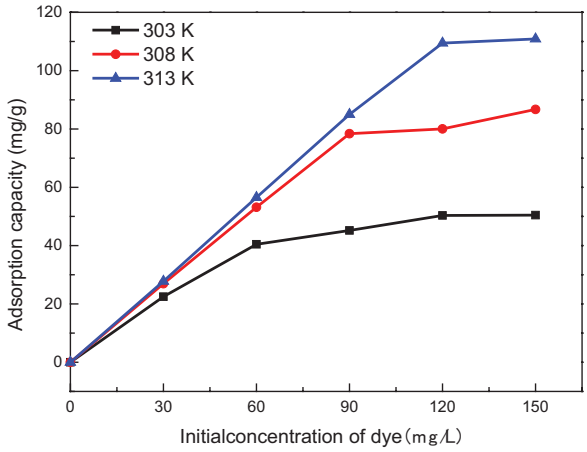

Fig.10. The adsorption curve at different dye initial concentration and temperature.

The thermodynamics parameters, such as ΔG, ΔS and ΔH, were calculated according to the adsorption equilibrium constant K_L as shown in Eqs. (14)–(16) [25,54,55].

$$\Delta G = -RT\ln K_L \quad (14)$$

Table 3
Adsorption kinetic constants and values

Temperature(K)	ΔG (KJ/mol)	ΔH (KJ/mol)	ΔS (J/K·mol)
305	–23.91	52.67	0.17
308	–21.74		
315	–19.54		

$$\Delta H = R\left[\frac{T_1 T_2}{T_1 - T_2}\right]\ln\left[\frac{K_{L2}}{K_{L1}}\right] \quad (15)$$

$$\lg K_L = \frac{\Delta S}{R} - \frac{\Delta H}{RT} \quad (16)$$

where K_{L1} and K_{L2} are constants of Langmuir isotherm model at temperature T_1 and T_2, respectively.

ΔG is negative at different temperatures, indicating that the adsorption process is spontaneous; ΔH is a positive value, indicating that the adsorption process is an endothermic reaction. A positive value of ΔS indicates that the chaos of the solid-liquid surface increases during the adsorption process of the nanocomposite on the Congo red dye.

4.Conclusion

In conclusion, an efficient, low cost method to synthesize C/$CoFe_2O_4$ nanocomposites was realized by double-membrane dispersion technology and hydrothermal carbonization method. Further studied showed that C/$CoFe_2O_4$ nanocomposites, as the new adsorbents, exhibited remarkable capacity for removing Congo red dyes in wastewater. Owing to the high yield and ability in removing dyes, this method by a simple blending method for the synthesis of C/$CoFe_2O_4$ nanocomposites is promising for future applications in removing persistent pollutants.

Acknowledgment

This project was financially supported by the National Natural Science Foundation of China (Nos. 51672040 and 51672013), Science and Technology Research Projects of the Education Department of Jilin Province (JJKH20180429KJ), Jilin City Science and Technology Bureau(201750228).

References

[1] R. Wang, X. Jin, Z. Wang, W. Gu, Z. Wei, A multilevel reuse system with source separation process for printing and dyeing wastewater treatment: A case study. Bioresource. Technol., 247 (2017) 1233–1241.
[2] A.A. Guedez, W. Püttmann, Printing ink and paper recycling sources of TMDD in wastewater and rivers, Sci. Total. Environ., 468 (2014) 671–676.
[3] L. Chen, R. Lei, P.F. Zhou, L.J. Liu, L.I. Wen, Research of upgrading and rebuilding to printing and dyeing wastewater by MBBR, Environ. Sci. Technol., 30 (2017) 39–42.
[4] J. Zeng, J. Liu, Economic model predictive control of wastewater treatment processes, Ind. Eng. Chem. Res., 54 (2015) 5710–5721.
[5] A.F. Gao, X.L. Liang, Y. Zhang, X.D. Han, J.H. Cui, Optimization of printing-ink wastewater treatment by fenton oxidation using response surface methodology, Environ .Sci. Technol., 36 (2013) 107–116.
[6] G. Zhen, X. Lu, T. Kobayashi, L. Su, G. Kumar, Continuous micro-current stimulation to upgrade methanolic wastewater biodegradation and biomethane recovery in an upflow anaerobic sludge blanket (UASB) reactor, Chemosphere, 180 (2017) 229–238.
[7] N. Birjandi, H. Younesi, A.A. Ghoreyshi, M. Rahimnejad, Electricity generation through degradation of organic matters in medicinal herbs wastewater using bio-electro-Fenton system, J. Environ. Manage., 180 (2016) 390–400.
[8] Y. Kim, B.E. Logan, Simultaneous removal of organic matter and salt ions from saline wastewater in bioelectrochemical systems, Desalination, 308 (2013) 115–121.
[9] S. Karthikeyan, A. Titus, A. Gnanamani, A.B. Mandal, G. Sekaran, Treatment of textile wastewater by homogeneous and heterogeneous Fenton oxidation processes, Desalination, 281 (2011) 438–445.
[10] M. Mehrjouei, S. Müller, D. Möller, A review on photocatalytic ozonation used for the treatment of water and wastewater, Chem. Eng. J., 263 (2015) 209–219.
[11] X.H. Xu, L.H. Zhang, Q.Y. Wang, M. Lu, X.Y. Meng, Study on absorbing Cu^{2+} by green adsorbent chlorella power, J. Northeast Electr. Pow. Uni., 34 (2014) 21–24.
[12] W. Wei, R. Lu, H. Xie, Y. Zhang, X. Bai, Selective adsorption and separation of dyes from an aqueous solution on organic-inorganic hybrid cyclomatrix polyphosphazene submicro-spheres, J. Mater. Chem. A., 3 (2015) 4314–4322.
[13] K.B. Tan, M. Vakili, B.A. Horri, P.E. Poh, A.Z. Abdullah, Adsorption of dyes by nanomaterials: Recent developments and adsorption mechanisms, Sep. Purif. Technol., 150 (2015) 229–242.
[14] M. Lu, X. Lu, F.Y. Li, X.H. Xu, C.Y. Yu, L.L. Yao, Thermodynamics and kinetics of adsorption of methylene blue by zeolite synthesized from fly ash, J. Northeast Electr. Pow. Uni., 34 (2014) 21–24.
[15] H.M. Marwani, H.M. Albishri, T.A. Jalal, E.M. Soliman, Study of isotherm and kinetic models of lanthanum adsorption on activated carbon loaded with recently synthesized Schiff's base, Arab. J. Chem., 10 (2017) 1032–1040.
[16] T. Zheng, Q. Wang, Z. Shi, Z. Zhang, Y. Ma, Microwave regeneration of spent activated carbon for the treatment of ester-containing wastewater, Rsc. Adv., 6 (2016) 60815–60825.
[17] A. Bhatnagar, W. Hogland, M. Marques, M. Sillanpää, An overview of the modification methods of activated carbon for its water treatment applications, Chem. Eng. J., 219 (2013) 499–511.
[18] L. Kong, X. Yin, F. Ye, Electromagnetic wave absorption properties of ZnO-based materials modified with $ZnAl_2O_4$ nanograins, J. Phys. Chem. C., 117 (2013) 2135–2146.
[19] J. Gómez-Pastora, E. Bringas, I. Ortiz, Recent progress and future challenges on the use of high performance magnetic nano-adsorbents in environmental applications, Chem. Eng. J., 256 (2014) 187–204.
[20] Y. Zhao, J. Li, S. Zhang, X. Wang, Amidoxime-functionalized magnetic mesoporous silica for selective sorption of U(VI), Rsc. Adv., 4 (2014) 32710–32717.
[21] N.P. Raval, P.U. Shah, N.K. Shah, Adsorptive amputation of hazardous azo dye Congo red from wastewater: a critical review, Environ. Sci. Pollut. Res. Int., 23 (2016) 14810–14853.
[22] V. Ranjithkumar, A.N. Hazeen, M. Thamilselvan, S. Vairam, Magnetic activated carbon-Fe_3O_4 nanocomposites - synthesis and applications in the removal of acid yellow dye 17 from water, J. Nanosci. Nanotechnol., 14 (2014) 1–11.
[23] A.M. Donia, A.A. Atia, F.I. Abouzayed, Preparation and characterization of nano-magnetic cellulose with fast kinetic properties towards the adsorption of some metal ions, Chem. Eng. J., 191 (2012) 22–30.
[24] L. Deng, Z. Shi, X. Peng, S. Zhou, Magnetic calcinated cobalt ferrite/magnesium aluminum hydrotalcite composite for enhanced adsorption of methyl orange, J. Alloy. Compd., 688 (2016) 101–112.

[25] X. Zhao, W. Wang, Y. Zhang, S. Wu, F. Li, Synthesis and characterization of gadolinium doped cobalt ferrite nanoparticles with enhanced adsorption capability for Congo Red, Chem. Eng. J., 250 (2014) 164–174.
[26] S. Joseph, D.M. Kempaiah, M. Benzigar, A.V. Baskar, S.N. Talapaneni, Metal organic framework derived mesoporous carbon nitrides with a high specific surface area and chromium oxide nanoparticles for CO_2 and hydrogen adsorption, J. Mater. Chem. A., 5 (2017) S1–S12.
[27] L.H. Ai, H.Y. Huang, Z.L. Chen, X. Wei, J. Jiang, Activated carbon/$CoFe_2O_4$, composites: Facile synthesis, magnetic performance and their potential application for the removal of malachite green from water, Chem. Eng. J., 156 (2010) 243–249.
[28] K.S. Thangamani, N.M. Andal, E.R. Kumar, M. Saravanabhavan, utilization of magnetic nano cobalt ferrite doped capra aegagrus hircus dung activated carbon composite for the adsorption of anionic dyes, J. Environ. Chem. Eng., 5 (2017) 2820–2829.
[29] L. Ai, M. Li, L. Li, Adsorption of methylene blue from aqueous solution with activated carbon/cobalt ferrite/alginate composite beads: kinetics, isotherms, and thermodynamics, J. Chem. Eng. Date., 56 (2011) 3475–3483.
[30] O. Oyetade, V. Nyamori, B. Martincigh, S. Jonnalagadda, Effectiveness of carbon nanotube-cobalt ferrite nanocomposites for the adsorption of rhodamine B from aqueous solutions, Rsc. Adv., 5 (2015) 22724–22739.
[31] A. Pirouzfar, S.A.S. Ebrahimi, Optimization of sol-gel synthesis of $CoFe_2O_4$ nanowires using template assisted vacuum suction method, J. Magn. Magn. Mater., 370 (2014) 1–5.
[32] M.Y. Nassar, K. Mai, Cobalt ferrite nanoparticles via a template-free hydrothermal route as an efficient nano-adsorbent for potential textile dye removal, Rsc Adv., 6 (2016) 79688–79705.
[33] E. Manova, B. Kunev, D. Paneva, I. Mitov, L. Petrov, Mechano-synthesis, characterization, and magnetic properties of nanoparticles of cobalt ferrite, $CoFe_2O_4$, Rsc. Adv., 16 (2016) 5689–5696.
[34] X.H. Guan, J.M. Kuang, H.B. Zhao, L. Yang, S.T. Li, Preparation of rGO/$CoFe_2O_4$ on membrane-hydrothermal method and wave absorbing properties, Chem. Ind. Eng. Prog., 34 (2015) 3693–3699.
[35] X.H. Guan, X. Wang, M. Lu, H.B. Zhao, Research of continuous preparation of nano-Fe_3O_4 based on membrane disperion technology, Mater. Rev., 27 (2013) 70–73.
[36] Z.G. Jia, D.P. Ren, R.S. Zhu, Synthesis, characterization and magnetic properties of $CoFe_2O_4$ nanorods, Mater. Lett., 66 (2012) 128–131.
[37] A.A. Sattar, H.M. El-Sayed, I. Alsuqia, Structural and magnetic properties of $CoFe_2O_4$/ $NiFe_2O_4$ core/shell nanocomposite prepared by the hydrothermal method, J. Magn. Magn. Mater., 395 (2015) 89–96.
[38] J.M. Gao, Z.K. Yan, J. Liu, M. Zhang, M. Guo, Synthesis, structure and magnetic properties of Zn substituted Ni–Co–Mn–Mg ferrites, Mater. Lett., 141 (2015) 122–124.
[39] M.P. Reddy, A.M.A. Mohamed, X.B. Zhou, S. Du, Q. Huang, A facile hydrothermal synthesis, characterization and magnetic properties of mesoporous $CoFe_2O_4$ nanospheres, J. Magn. Magn. Mater., 388 (2015) 40–44.
[40] P.R. Kumar, P. Kollu, C. Santhosh, K.E.V. Rao, D.K. Kim, A.N. Grace, Enhanced properties of porous $CoFe_2O_4$-reduced graphene oxide composites with alginate binders for Li-ion battery applications, New J. Chem., 38 (2014) 3654–3661.
[41] L. Deng, Z. Shi, X. Peng, Adsorption of Cr(VI) onto a magnetic $CoFe_2O_4$/MgAl-LDH composite and mechanism study, Rsc. Adv., 5 (2015) 49791–49801.
[42] V. Hermán, H. Takacs, F. Duclairoir, O. Renault, J.H. Tortai, Core double–shell cobalt/graphene/polystyrene magnetic nanocomposites synthesized by in situ sonochemical polymerization, Rsc. Adv., 5 (2015) 51371–51381.
[43] W. Chen, L. Yan, P.R. Bangal, Preparation of graphene by the rapid and mild thermal reduction of graphene oxide induced by microwaves, Carbon, 48 (2010) 1146–1152.
[44] I. Ali, C. Peng, I. Naz, Z.M. Khan, M. Sultan, T. Islam, I.A. Abbasi, Phytogenic magnetic nanoparticles for wastewater treatment: a review, Rsc. Adv., 7 (2017) 40158–40178.
[45] L. Wang, J. Li, Y. Wang, L. Zhao, Q. Jiang, Adsorption capability for Congo red on nanocrystalline MFe_2O_4 (M = Mn, Fe, Co, Ni) spinel ferrites, Chem. Eng. J., 181–182 (2012) 72–79.
[46] V. Poonam, C. Pratibha, K. Atul, Removal of reactive orange 107 dye from textile effluent by adsorption on acid treated fly ash, Res. J. Chem. Environ., 18 (2014) 12–21.
[47] A. Poorbafrani, E. Kiani, Enhanced microwave absorption properties in cobalt-zinc ferrite based nanocomposites, J. Magn. Magn. Mater., 416 (2016) 10–14.
[48] P. Cai, H.G. Zheng, C. Wang, H.W. Ma, J.C. Hu, Y.B. Pu, P. Liang, Competitive adsorption characteristics of fluoride and phosphate on calcined Mg–Al–CO_3 layered double hydroxides, J. Hazard. Mater., 213–214 (2012) 100–108.
[49] T. Jiang, Y.D. Liang, Y.J. He, Q. Wang Activated carbon/$NiFe_2O_4$ magnetic composite: A magnetic adsorbent for the adsorption of methyl orange, J. Environ. Chem. Eng., 3 (2015) 1740–1751.
[50] H. Chen, J. Zhao, G.L. Dai, J.Y. Wu, H. Yan, Adsorption characteristics of Pb(II) from aqueous solution onto a natural biosorbent, fallen Cinnamomum camphora leaves, Desalination, 262 (2010) 174–182.
[51] K.Y. Shin, J.Y. Hong, J. Jang, Heavy metal ion adsorption behavior in nitrogen-doped magnetic carbon nanoparticles: isotherms and kinetic study, J. Hazard. Mater., 190 (2011) 36–44.
[52] J. Gómez-Pastora, E. Bringas, I. Ortiz, Recent progress and future challenges on the use of high performance magnetic nano-adsorbents in environmental applications, Chem. Eng. J., 256 (2014) 187–204.
[53] M. Lu, Y.M. Zhang, X.H. Guan, X.H. Xu, T.T. Gao, Thermodynamics and kinetics of adsorption for heavy metal ions from aqueous solutions onto surface amino-bacterial cellulose, Nonferr. Metal. Soc., 24 (2014) 1912–1917.
[54] P. Zhang, T. Wang, G. Qian, D. Wu, R.L. Frost, Removal of methyl orange from aqueous solutions through adsorption by calcium aluminate hydrates, Interf. Sci., 426 (2014) 44–47.
[55] X. Yuan, Y. Wang, J. Wang, C. Zhou, Q. Tang, Calcined graphene/MgAl-layered double hydroxides for enhanced Cr(VI) removal, Chem. Eng. J., 221 (2013) 204–213.

Supporting information

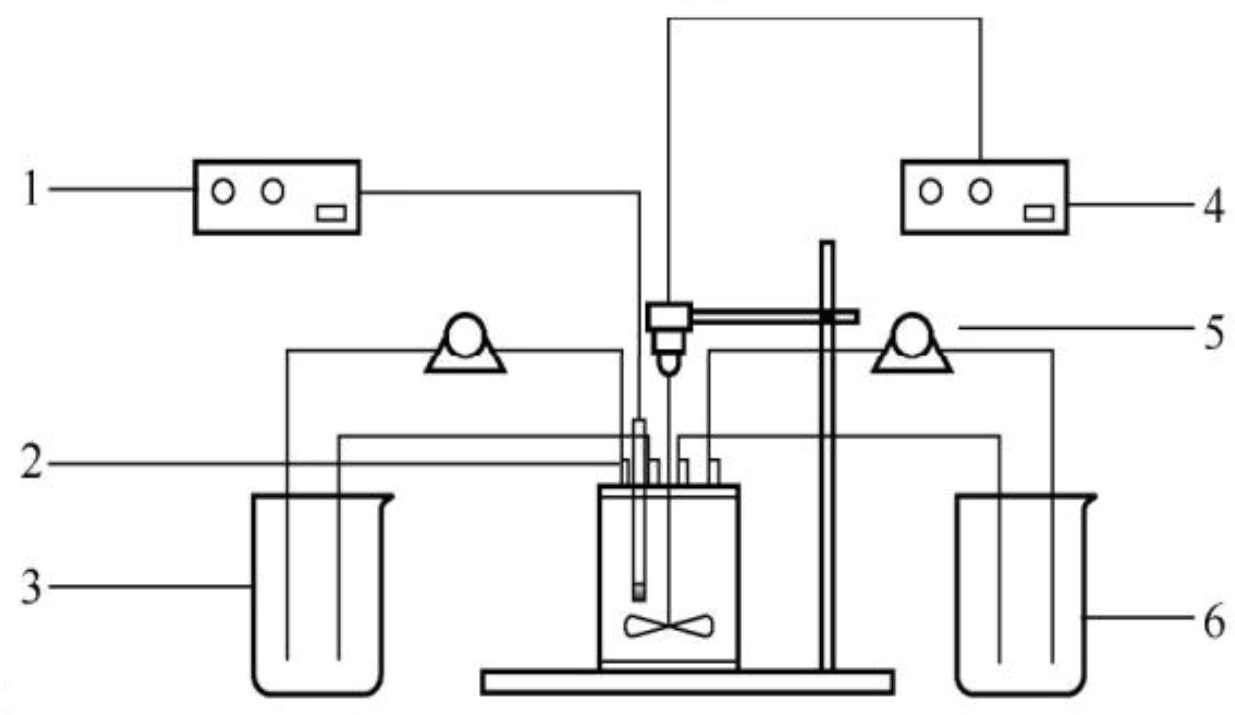

Fig. S1. Device for preparing $CoFe_2O_4$ precursor by double membrane dispersion method pH meter; 2-membrane module; 3-Fe^{3+}, Co^{2+} mixture; 4-force electric stirrer; 5-peristaltic pump; 6-$H_2C_2O_4$ solution.

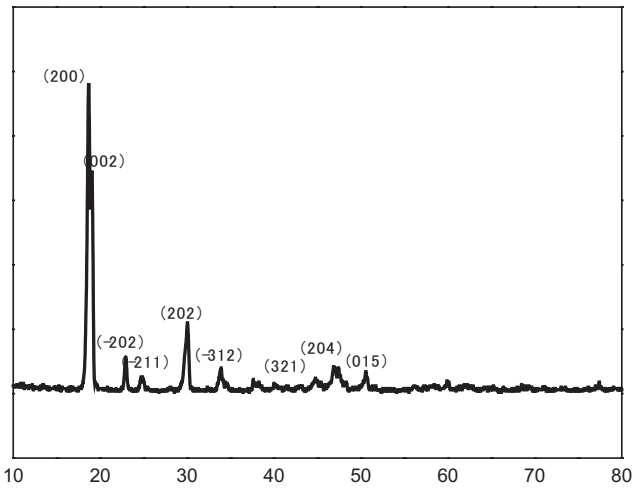

Fig. S2. XRD pattern of $CoFe_2(C_2O_4)_3$ precursor.

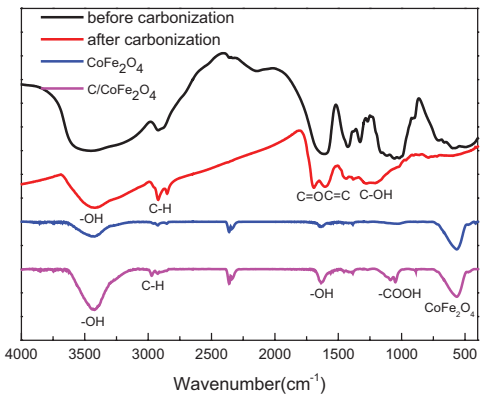

Fig. S3. FT-IR spectra of CMC, $CoFe_2O_4$ and nanocomposites.

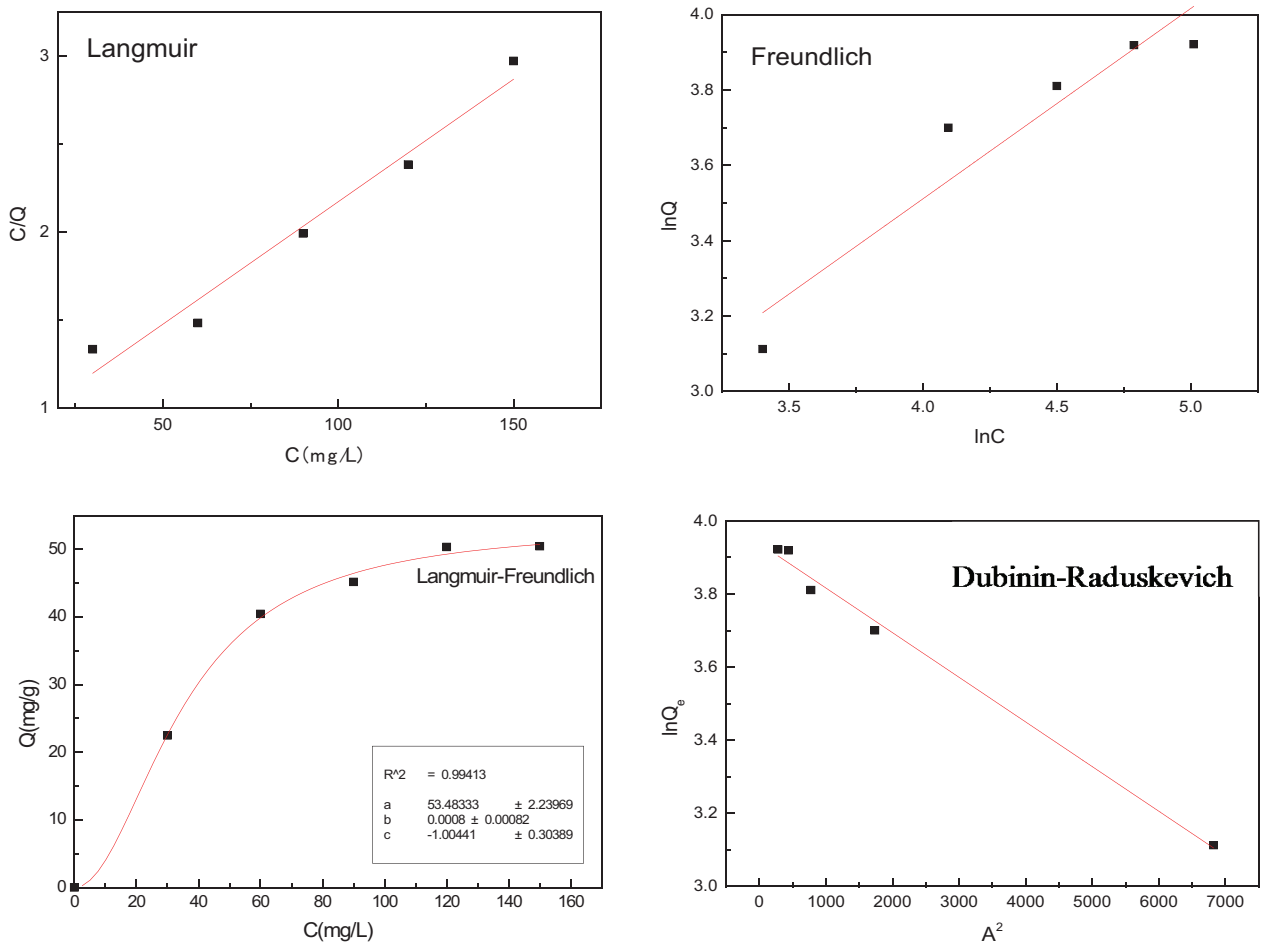

Fig. S4. Isothermal Line model of Congo red adsorbed on nanocomposites.